Universiteit Antwerpen

This item is the archived peer-reviewed author-version of:

Thermodynamics at the nanoscale : phase diagrams of nickel-carbon nanoclusters and equilibrium constants for face transitions

Reference:

Thermodynamics at the nanoscale: Phase diagrams of nickel-carbon nanoclusters and equilibrium constants for phase transition

Yannick Engelmann,[*a] **Annemie Bogaerts,**[b] **and Erik C. Neyts**[b]

Using reactive molecular dynamics simulations, the melting behavior of nickel-carbon nanoclusters is examined. The phase diagrams of icosahedral and Wulff polyhedron clusters are determined using both the Lindemann index and the potential energy. Formulae are derived for calculating the equilibrium constants and the solid and liquid fractions during a phase transition, allowing a more rational determination of the melting temperature with respect to the arbitrary Lindemann value. These results give more insight into the properties of nickel-carbon nanoclusters in general and can specifically be very useful for a better understanding of the synthesis of carbon nanotubes using the catalytic chemical vapor deposition method.

1 Introduction

Carbon nanotubes (CNTs) are envisaged for a wide variety of applications, including electronics, material science, medical applications and more[1]. A lot of research is therefore conducted in search of an effective synthesis method for carbon nanotubes that is also able to control the properties of the tubes produced. One of the most often used synthesis methods is the catalytic chemical vapor deposition (CCVD) method. Here, a hydrocarbon source gas is catalytically decomposed on the surface of a nanoparticle, allowing the carbon atoms to dissolve in the nanocluster. Upon supersaturation, the carbon atoms segregate to the surface where they bind to each other and eventually grow into a solid nanotube. It is believed that this growth mechanism is strongly dependent on the physical state of the cluster. Due to the Gibbs-Thomson effect[2–4], nanoclusters melt at lower temperatures than their bulk counterparts. At the temperatures used in CCVD, typically in the order of 1000K, the cluster may thus be liquid, semi-liquid, or solid, depending on the exact catalyst material, shape and size. Clearly, a good understanding of the melting behavior of the nanocluster is essential.

The melting behavior can be examined through various methods, including calculating the average potential energy of the cluster and the interatomic distances during a number of MD steps, or by calculating some order parameter, like for instance the Lindemann index[3,5–7]. Since in liquids, atoms can move further from their equilibrium positions than in solids,

their average potential energy will higher. The melting behavior of a system can thus be derived from a plot of the potential energy as a function of temperature.

The Lindemann index is defined as:

$$\delta = \frac{2}{N(N-1)} \sum_{i<j} \frac{\sqrt{<r_{ij}^2> - <r_{ij}>^2}}{<r_{ij}>} \quad (1)$$

where N is the number of atoms, and r_{ij} is the interatomic distance between atoms i and j. Since atoms in liquids can move more freely than in solids, the Lindemann index typically has low values for solids and higher values for liquids. The temperature at which the Lindemann index has a sudden increase, can thus be called the melting point. The Lindemann index for bulk materials will therefore look like the step function, with the discontinuity at the melting point. It is actually not exactly a step function, since the Lindemann index is also a function of temperature (increasing temperature will cause lattice expansion and an increase in atomic motion) and so the horizontal lines will actually have a slope slightly higher than zero. The Lindemann index for nanoclusters does not show this discontinuity, it rather shows a temperature interval where the index will gradually increase. The Lindemann index has, inter alia, been applied to a variety of nanoclusters, including nickel[6,7], iron[3,5,8], silicon[9] and molybdenum[10]. At the macroscopic scale, fcc nickel has a melting temperature of 1724K[6], while at the nanoscale melting occurs at significantly lower temperatures. For a bulk system the number of atoms at the surface is negligible compared to the total number of atoms, while for nanostructures the number of atoms at the surface is of the same order of magnitude as the total number of atoms. Therefore, also the surface energy has to be taken into account. This affects the thermodynamical proper-

a Research Group PLASMANT, Department of Chemistry, University of Antwerp, Universiteitsplein 1, 2610, Antwerp, Belgium; E-mail: yannick.engelmann@student.kuleuven.be
b Research Group PLASMANT, Department of Chemistry, University of Antwerp, Universiteitsplein 1, 2610, Antwerp, Belgium

ties of the system and these effects are generally referred to as the Gibbs-Thomson phenomenon[2–4]. Also, when carbon atoms are dissolved in the cluster it partially breaks the crystal lattice, thus lowering the melting point even more[11].

As mentioned above, nanoclusters have a melting interval rather than a melting point. In this interval the cluster can be found in either a liquid or a solid state. More specifically, at a fixed temperature within the melting interval, the smaller nanoclusters show phase fluctuations in time[3,6,8]. These fluctuations may easily take more than a few nanoseconds making traditional MD simulations of this process practically impossible. In order to deal with this problem, we here combine MD simulations with force bias Monte Carlo simulations[12–14], which allows a much faster sampling of configuration space.
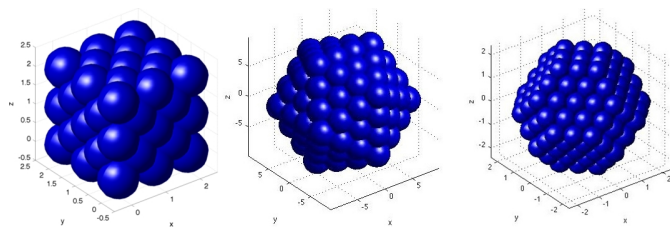

Fig. 1 Crystal structures of nickel: (a) a bulk fcc lattice; (b) an icosahedral cluster (147 atoms), and (c) a Wulff polyhedron (201 atoms)

Bulk nickel, in its most stable form, has an fcc lattice, with a lattice parameter of 3.52Å[15,16]. At the nanoscale, nickel clusters appear with different geometries depending on their number of atoms. Two often observed geometries are the icosahedron and the Wulff polyhedron, shown in Fig. 1. In this contribution, we calculate the phase diagrams for the smallest clusters of these two (often occurring) geometries.

The bulk Ni/C phase diagram is shown in Fig. 2[17]. The different regions in this diagram represent the equilibrium states of a nickel-carbon cluster as a function of concentration and temperature. For example, at 2000 °C, a system with 50% carbon is not stable and will decompose into a liquid state with a carbon concentration of about 30% and a state of pure graphite. At about 1327 °C one observes the eutectic line. A system on this line, will decompose into a triple-state system (a solid state consisting of nickel and carbon, a solid state of pure graphite and a liquid state of nickel and carbon). The concentration of this liquid state determines the eutectic point. At the nanoscale, the phase diagram depends both on the cluster size and the geometry of the cluster. The melting interval in a phase diagram of a bulk structure denotes the existence of a double-state system. In this case, melting intervals for nanoclusters should be interpreted differently. Because of their small sizes, fluctuations in a small part of the cluster will im-
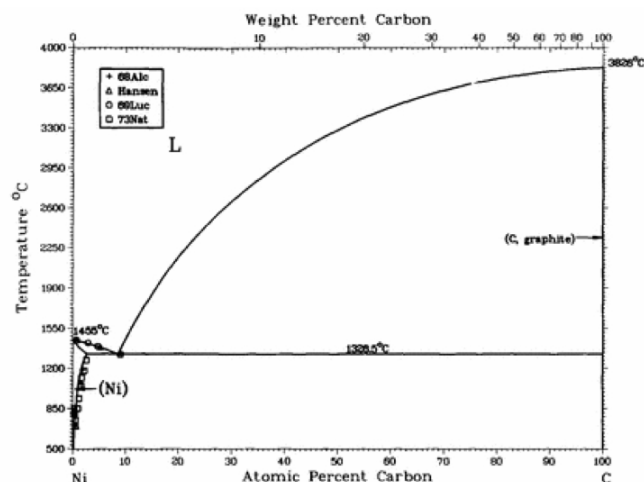

Fig. 2 Phase diagram of a nickel-carbon system at the macroscale

mediately affect the rest of the cluster. This makes it impossible for a cluster to have both a liquid and a solid part at the same time. Therefore, the notion of a double-state system in the classical way, has no meaning at the nanoscale. The physical state of the cluster might change as a function of time, so that we could say that there is a double-state system in time, instead of in space. We here propose that in order to denote how long a nanocluster is in the solid or liquid state, one can make use of an equilibrium constant K, where:

$$K = \frac{time\ in\ liquid\ state}{time\ in\ solid\ state} \qquad (2)$$

Ideally, this value is zero for temperatures well beneath the melting interval (i.e., the cluster is always solid) and infinite at values well above the melting interval (i.e., the cluster is always liquid, ignoring the liquid-gas phase transition). Within the melting interval, K will increase with increasing temperature.

2 Simulation Setup

To perform the calculations we made use of molecular dynamics and Monte Carlo simulations which let the nanoclusters evolve through the configuration space. During the various steps in these simulations several instantaneous values are calculated, like the distances between the atoms in the cluster, the potential energy and the kinetic energy. Subsequently, these values can be used to calculate time average quantities and order parameters, like the Lindemann index, to describe the properties of the observed nanoclusters. The actual calculations consist of an equilibration stage, followed by a stage calculating the Lindemann index and the potential

energy. The equilibration part is used to let the nanocluster evolve towards a stable configuration before the actual calculations begin. This is done by alternating between MD and fbMC simulations. The fbMC steps guide the atoms of the nickel-carbon cluster towards stable positions in configuration space, while the MD steps are used to equilibrate the temperature of the cluster. For the different nickel-carbon clusters, we used an icosahedral or Wulff polyhedron starting lattice for the nickel atoms. If at a certain temperature or carbon concentration a different configuration, like e.g. a decahedron, is more stable, the fbMC steps will guide the cluster to this configuration. In the actual calculation stage, the nanoclusters are followed for 2.10^6 MD steps with a time step of 0.25 fs, again regularly alternated with fbMC steps. After every fbMC cycle the velocities are re-equilibrated during 2000 MD steps before calculating the interatomic distances as well as the potential energy of the cluster. Subsequently a new fbMC cycle starts. To control the temperature throughout the calculations we made use of the Bussi thermostat, generating the canonical ensemble[18]. Energies and forces on the atoms are calculated using the ReaxFF potential[19]. ReaxFF is an empirical force field where the link between the energy and the geometry of the cluster is given by a superposition of different energy contributions[15,20], which are constructed such that not only covalent bonding can be described, but also Coulomb and van der Waals interactions, which allows to take into account interactions at longer distances[20]. The ReaxFF parameters for Ni/C were developed by fitting against a large body of quantum mechanical (QM) data. The Ni-Ni parameters were fitted against QM heats of formation for nickel at various densities in fcc, bcc, a15, simple cubic, and diamond crystal structures as calculated with QM. C/Ni (as well as H/Ni) parameters were fitted against QM binding energies for hydrocarbons at nickel surface, subsurface, and bulk sites, as well as against QM heats of formation for Ni_3C, Ni_2C, and the B1, B2, B3, and B4 phases of NiC. This extensive fitting data set, together with the force fields ability to reproduce properties relevant to the Ni/C system that were not included in the fitting database, demonstrates the applicability of Reax to the studied system. Chemical bonds can be formed and broken in this force field, making it possible for the atoms to leave their equilibrium lattice positions. A more exact description of the different terms are explained in the references, and the references therein[15,20].

3 Results and discussion

An example of a calculated Lindemann index curve and a potential energy curve using the methodology described above is shown in Fig. 3. From these curves, the lower and upper limit of the melting interval are deduced (see below) and drawn in the phase diagrams.

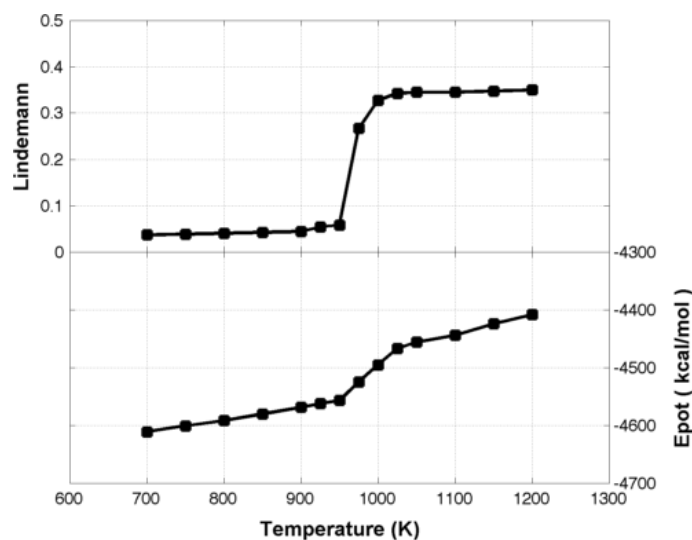In Fig. 4, we show the phase diagrams for the nickel-carbon

Fig. 3 Calculated Lindemann index and potential energy curve of the icosahedral Ni_{55} nanocluster

system for the 4 smallest icosahedral clusters and the 4 smallest Wulff polyhedrons. We note the presence of a melting interval with a magnitude ranging roughly from 50 to 500 K, depending on the size of the cluster, the geometry of the cluster and the carbon concentration. Specifically, the melting interval increases with increasing carbon concentration, is somewhat larger for the Wulff clusters, and decreases with increasing cluster size. For the bulk diagram a eutectic point exists around a carbon concentration of about 10%, denoting a concentration (different from 0% and 100%) where the system does not have a melting interval but a melting point. The nanoclusters, on the other hand, show a melting interval for all carbon concentrations examined. When looking at the upper bound of the melting interval, we see that, starting from the pure Ni-cluster, the temperature decreases with increasing carbon concentration until a minimum around 10% carbon, after which it increases again. This trend is more clear for the icosahedral clusters than for the Wulff polyhedrons. This is comparable to the macroscopic system, where a similar trend can be observed, and where the minimum corresponds to the eutectic point which can also be found at a carbon concentration of about 10%. Upon inspection of the lower limit of the melting intervals, we can see that for all clusters, the corresponding temperature is at a maximum for the pure state, decreases with increasing carbon concentration and stays constant at higher concentrations. We could therefore conclude that there exists a eutectic line just like in the case of a bulk system. Additionally, we also note that the phase diagrams can be significantly different for different cluster sizes and different cluster geometries. Firstly, we notice that the smaller clus-
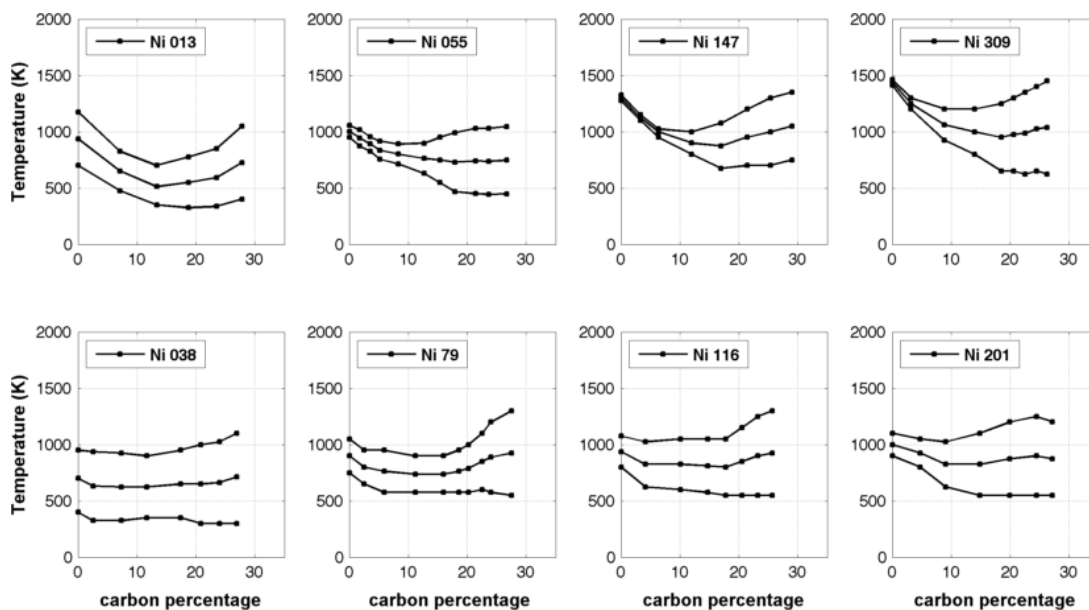
Fig. 4 Nickel-Carbon phase diagrams of icosahedral clusters (top series) and Wulff polyhedrons (lower series). The lower line depicts the temperature where the liquid fraction is 5%, the middlemost line depicts the temperature where the liquid fraction is 50% and the upper line depicts the temperature where the liquid fraction is 95%. The number of nickel atoms in the clusters is shown on the top left corner of each graph.

ters have wider melting intervals than the bigger clusters, as expected, since thermodynamic fluctuations have higher impact on small clusters than on large clusters. Secondly, at low carbon concentrations, we observe larger melting intervals for the Wulff polyhedrons compared to the icosahedral clusters, which means that fluctuation amplitudes are greater in an fcc lattice than in a Mackay icosahedron. At larger concentrations, this difference vanishes since the fcc lattice and icosahedral lattice become more and more distorted. When we look at the pure clusters (the values corresponding to 0% carbon) we can see that the melting point increases with the number of atoms. This phenomenon is well known in literature and a linear dependence of the melting point on the inverse diameter of the cluster is suggested in several papers[3,6,10,21]. Finally, we note that the phase diagrams for the icosahedrons seem to be more dependent on the cluster size than the phase diagrams for the Wulff polyhedrons. Due to the absence of shells in the latter, carbon atoms can move more freely inside the nanoparticle, as will be shown further on in the section on the structures of the clusters. Consequently, also the melting behavior will depend less on the size of the cluster.

For the derivation of the equilibrium constant we consider an isothermal process starting in the solid state and moving to an equilibrium state with liquid fraction y and solid fraction x. This transition is shown in Fig. 5 by the arrow ΔU. We emphasize again that the liquid fraction and solid fraction are the
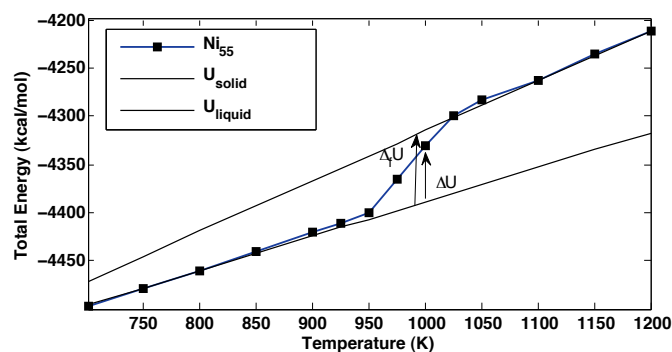

Fig. 5 Total energy curve of the Ni_{55} nanocluster.

time fractions of the cluster being in a liquid state or a solid state. One should also realize that the traditional principles of thermodynamics are not to be applied to nanosystems without serious consideration[22]. In this case, however, we choose to work with the change in Gibbs free energy since we are looking for time averaged values, and not instantaneous values. The lower straight line in Fig. 5 denotes the total energy of the solid cluster as a function of temperature, the upper straight line the total energy of the liquid cluster as a function of temperature and the full line denotes the results obtained from

the calculations. Note that the solid and liquid line imply an extrapolation to higher/lower temperatures. However, the relative stability of the different structures of nanoparticles (including the equilibrium structure) is function of temperature and thus extrapolation should take these changes into account. In our simulations, the correct relative stability of the different states is achieved by the implemented MC steps, as explained above.

Since in our simulation the external pressure is constant (and equal to zero), the minimum in Gibbs free energy will determine the point of equilibrium. We are thus looking for the solution to the equation:

$$0 = \Delta H - T\Delta S \qquad (3)$$

The enthalpy H is defined as U + pV, with p equal to zero, so that H equals U. One then finds (along with the definition of entropy):

$$0 = \Delta U - T \int_i^f \frac{\delta Q}{T} \qquad (4)$$

Since the system fares in isobaric surroundings, and since only a fraction y melts, this leads us to:

$$0 = \Delta U - T . \frac{y\Delta_f H}{T} \qquad (5)$$

Where $\Delta_f H$ is the enthalpy of fusion shown in Fig. 5 as $\Delta_f U$, since for zero pressure H equals U. Consequently, the liquid fraction y is given by:

$$y = \frac{\Delta U}{\Delta_f U} \qquad (6)$$

and the solid fraction x is given by:

$$x = \frac{\Delta_f U - \Delta U}{\Delta_f U} \qquad (7)$$

where $x + y = 1$. We conclude that the equilibrium constant K (= y/x) is:

$$K = \frac{\Delta U}{\Delta_f U - \Delta U} \qquad (8)$$

showing the ratio of the liquid and solid fractions as an average in time. One can easily see that for temperatures well beneath the melting interval, ΔU equals zero, causing y to be 0 and x to be 1, and analogously we see that for temperatures well above the melting interval y will become 1 and x will become 0, since in these regions ΔU equals $\Delta_f U$.

To apply this to our calculations we construct the internal energy lines of the solid and the liquid system. In particular we calculate the total energy for several temperatures well below the melting interval ($x = 1$) and fit these results to a first order polynomial, and then the same is done for temperatures well above the melting interval ($y = 1$). The result are the
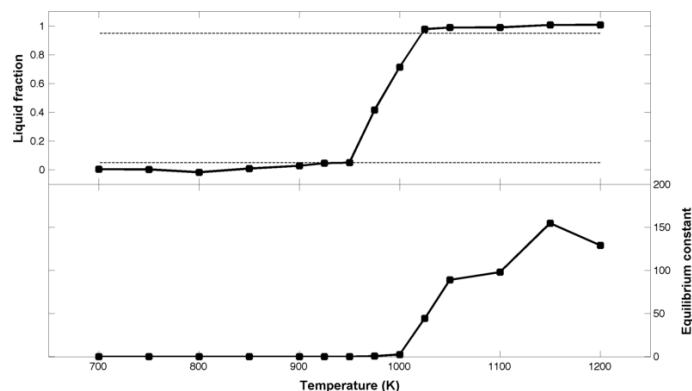

Fig. 6 Calculated liquid fraction and equilibrium constant of the icosahedral Ni_{55} nanocluster. The dashed lines in the upper plot represent a liquid fraction of 5% and 95%

two straight lines in Fig. 5. Subsequently we can calculate ΔU and $\Delta_f U$ for any temperature, as shown in the picture, by subtracting the value of the fitted solid line from the total energy obtained through our calculations at that temperature. Then we can calculate K, y and x with the formulae above.

Fig. 6 shows the calculated liquid fraction y and the equilibrium constant K as a function of temperature for the Ni_{55} icosahedral nanocluster. The dashed lines in the upper plot represent a liquid fraction of 5% ($y = 0.05$) and of 95% ($y = 0.95$). The intersections with the calculated liquid fraction are then chosen to be the start and the end of the melting interval. This method gives a more intuitive alternative to the often vaguely determined melting points in the literature. From the plot of the equilibrium constant, we can for example conclude that at a temperature of 800K, the cluster is almost constantly solid ($K = 0$) while at 1150K the cluster will be approximately 150 times longer in the liquid state than in the solid state ($K = 150$).

Finally, we also discuss the structure of the examined nickel-carbon nanoclusters. For this we make use of an adapted Radial Distribution Function (RDF). Usually, to construct a traditional RDF, one starts by calculating all interatomic distances between the atoms in the system and the number of atoms in the range from r to $r + dr$ is then put in a graph. An RDF is useful for the description of interatomic distances but in the following we will try to depict the entire structure of the nanoclusters. Fig. 7 displays the average structure of the $Ni_{147}C_5$ icosahedral cluster. The graphs show the distances from the atoms to the central atom of the cluster. These graphs are constructed in a similar way as a traditional RDF, except that instead of considering all interatomic distances, we here consider only the distance from the atoms to the central atom of the cluster. For comparison, the first graph in Fig. 7 shows the structure of the pure Ni_{147} icosahedral
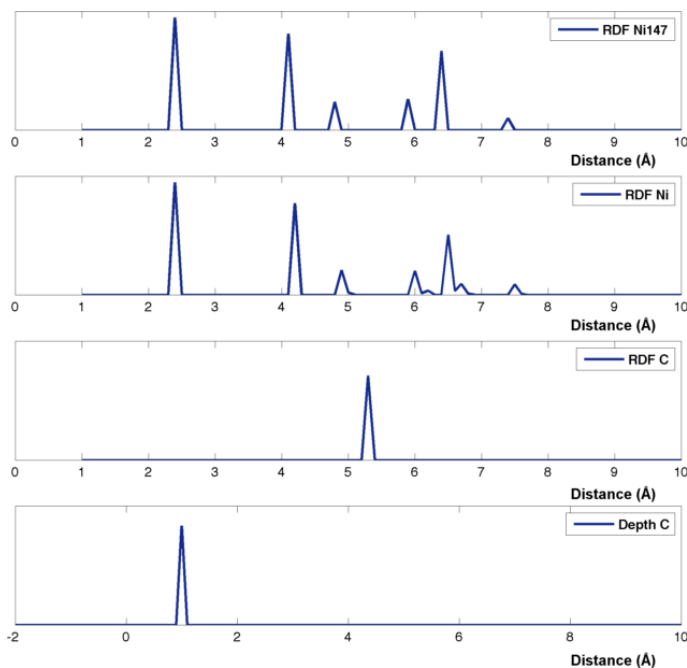
Fig. 7 From top to bottom, RDF of a) Ni in Ni_{147} (Icosahedron); b) Ni in $Ni_{147}C_5$; c) C in $Ni_{147}C_5$ and d) the depth of C in $Ni_{147}C_5$ Distances are calculated with respect to the central atom

Fig. 8 From top to bottom, RDF of a) Ni in Ni_{147} (Icosahedron); b) Ni in $Ni_{147}C_{40}$; c) C in $Ni_{147}C_{40}$ and d) the depth of C in $Ni_{147}C_{40}$ Distances are calculated with respect to the central atom

cluster. We can distinguish 1 peak for the first shell, 2 peaks for the second shell and 3 peaks for the third. The second graph shows the positions of the nickel atoms in the $Ni_{147}C_5$ cluster. We ascertain that the inner shells remain perfectly intact and that there are only small distortions in the outer shell. The third graph shows the distance of the carbon atoms to the central atom. When we compare this to the previous graph we can clearly see that the carbon atoms are situated between the second and the third shell, and thus not in the shells themselves. At higher concentrations, see Fig. 8, we can still distinguish the original nickel lattice, although the structure is much more distorted, the innermost shells remain always intact and the carbon atoms are still mostly found in between the shells, but some carbon atoms are positioned deeper into the cluster or sometimes attached to the surface. In Fig. 9 we display the average structure of the $Ni_{201}C_{20}$ Wulff polyhedron. It is important to notice that the carbon atoms can position themselves more freely than in icosahedrons because of the absence of shells. This explains, as mentioned above, why the melting behavior of a Wulff polyhedron depends much less on the size of the cluster, compared to icosahedrons. Since the carbon atoms can move more freely inside the nanoparticle, their positions are much less influenced by the size of the cluster. Consequently, also the melting behavior will depend less on the size of the cluster.
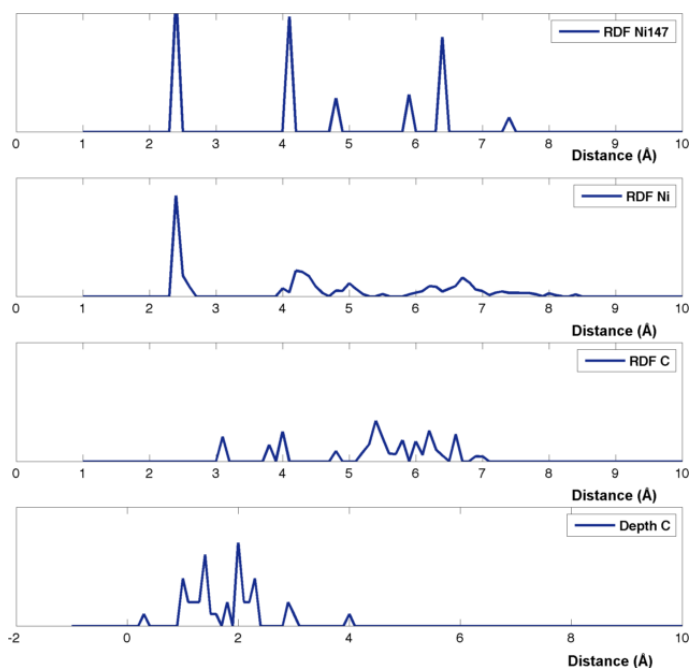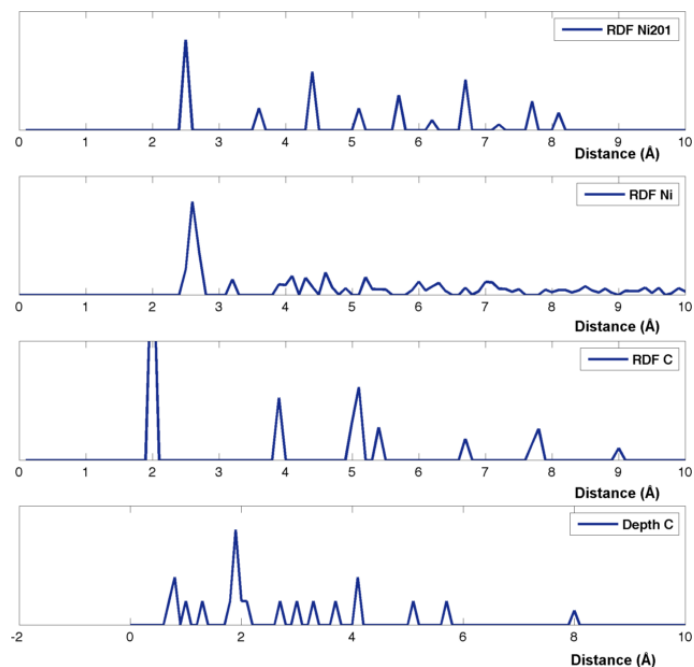

Fig. 9 From top to bottom, RDF of a) Ni in Ni_{201} (Wulff polyhedron); b) Ni in $Ni_{201}C_{20}$; c) C in $Ni_{201}C_{20}$ and d) the depth of C in $Ni_{201}C_{20}$ Distances are calculated with respect to the central atom

4 Conclusions

In conclusion, we calculated the phase diagrams of the four smallest icosahedral as well as the four smallest Wulff polyhedron nickel-carbon clusters using combined MD/MC simulations. The results are derived from the Lindemann index of the atoms and the potential energy of the clusters. The results show that both the geometry and the size of the cluster have a significant influence on the melting behaviour. The icosahedral clusters show different phase diagrams than the Wulff polyhedrons. Moreover, the size of the cluster also influences the width of the melting interval. One can distinguish a eutectic line similar to the macroscopic system. Although no real eutectic point is observed, one does observe a minimum in the upper bound of the melting interval around the same carbon concentration as the eutectic point at the macroscale. This kind of knowledge is obviously very important if we want to examine the influence of the crystal structure on the growth mechanism of carbon nanotubes with the CCVD method or if one wants to examine the carbon diffusion rate for different geometries, at different temperatures. Furthermore, we introduced a method to calculate time averaged liquid and solid fractions and an equilibrium constant as a function of temperature. These quantities give a better understanding of the existing phase oscillations of the clusters in time and can also be used to determine their melting intervals.

In general these results give more insight on the thermodynamic and structural properties of nanoclusters. The liquid and solid fractions and equilibrium constants can be useful tools for the description of the clusters. And finally the phase diagrams can be used for optimising synthesis mechanisms (as for example the growth of carbon nanotubes) and to explain experimental observations.

Acknowledgements

References

1 R. H. Baugman, *Science*, 2002, **297**, 787–792.
2 R. Overney, *NME*, 2010, **498**,.
3 A. Jiang, N. Awasthi, A. N. Kolmogorov, W. Setyawan, A. Börjesson, K. Bolton, A. R. Harutyunyan and S. Curtarolo, *Phys. Rev. B*, 2007, **75**, 205426.
4 R. Hashimoto, Y. Shibuta and T. Suzuki, *ISIJ International*, 2011, **51**, 1664–1667.
5 O. S. Vaulina, S. V. Vladimirov, O. F. Petrov and V. E. Fortov, *Phys. Rev. Lett.*, 2002, **88**, 245002.
6 E. Neyts and A. Bogaerts, *J. Phys. Chem. C*, 2009, **113**, 2771–2776.
7 A. J. Page, H. Yamane, Y. Ohta, S. Irle and K. Morokuma, *Journal of the American Chemical Society*, 2010, **132**, 15699–15707.
8 H. Duan, F. Ding, A. Rosn, A. R. Harutyunyan, S. Curtarolo and K. Bolton, *Chemical Physics*, 2007, **333**, 57 – 62.
9 D. Kang, Y. Hou, J. Dai and J. Yuan, *Phys. Rev. A*, 2009, **79**, 063202.
10 Y. Shibuta and T. Suzuki, *Phys. Chem. Chem. Phys.*, 2010, **12**, 731–739.
11 E. Neyts, Y. Shibuta, A. C. T. van Duin and A. Bogaerts, *ACS Nano*, 2010, **4**, 6665–6672.
12 M. Timonova, J. Groenewegen and B. J. Thijsse, *Phys. Rev. B*, 2010, **81**, 144107.
13 E. C. Neyts, B. J. Thijsse, M. J. Mees, K. M. Bal and G. Pourtois, *Journal of Chemical Theory and Computation*, 2012, **8**, 1865–1869.
14 M. J. Mees, G. Pourtois, E. C. Neyts, B. J. Thijsse and A. Stesmans, *Phys. Rev. B*, 2012, **85**, 134301.
15 J. E. Mueller, A. C. van Duin and W. A. Goddard, *J. Phys. Chem. C*, 2010, **114**, 4939–4949.
16 N. N. Lathiotakis, A. N. Andriotis, M. Menon and J. Connolly, *J. Chem. Phys.*, 1996, **104**, 992.
17 M. Singleton and P. Nash, *Bulletin of Alloy Phase Diagrams*, 1989, **10**, 121–126.
18 G. Bussi, D. Donadio and M. Parrinello, *J. Chem. Phys.*, 2007, **126**, 014101.
19 A. C. T. van Duin, S. Dasgupta, F. Lorant and W. A. Goddard, *The Journal of Physical Chemistry A*, 2001, **105**, 9396–9409.
20 E. C. Neyts, Y. Shibuta and A. Bogaerts, *Chemical Physics Letters*, 2010, **488**, 202–205.
21 A. Lyalin, A. Hussien, A. V. Solov'yov and W. Greiner, *Phys. Rev. B*, 2009, **79**, 165403.
22 M. Horodecki and J. Oppenheim, *Nature Communications*, 2013, **4**, 2059.
23 M. Diarra, H. Amara, F. Ducastelle and C. Bichara, *physica status solidi (b)*, 2012, **249**, 2629–2634.
24 M. Diarra, A. Zappelli, H. Amara, F. Ducastelle and C. Bichara, *Phys. Rev. Lett.*, 2012, **109**, 185501.
25 Y. Hou, H. Kondoh, T. Ohta and S. Gao, *Applied Surface Science*, 2005, **241**, 218 – 222.
26 T. L. Hill, *Nano Letters*, 2001, **1**, 273–275.